Propagation of statistical uncertainties of Skyrme mass models to simulations of *r*-process nucleosynthesis

T. M. Sprouse,[1,2] R. Navarro Perez,[3] R. Surman,[1] M. R. Mumpower,[2] G. C. McLaughlin,[4] and N. Schunck[5]

[1]*Department of Physics, University of Notre Dame, Notre Dame, Indiana 46556, USA*
[2]*Theoretical Division, Los Alamos National Laboratory, Los Alamos, New Mexico 87545, USA*
[3]*Department of Physics, San Diego State University, San Diego, California 02182, USA*
[4]*Department of Physics, North Carolina State University, Raleigh, North Carolina 27695, USA*
[5]*Nuclear and Chemical Science Division, Lawrence Livermore National Laboratory, Livermore, California 94551, USA*

(Received 16 January 2019; revised manuscript received 2 September 2019; accepted 2 April 2020; published 15 May 2020)

Uncertainties in nuclear models have a major impact on simulations that aim at understanding the origin of heavy elements in the universe through the rapid neutron capture process (*r* process) of nucleosynthesis. Within the framework of the nuclear density functional theory, we use results of Bayesian statistical analysis to propagate uncertainties in the parameters of energy density functionals to the predicted *r*-process abundance pattern, by way not only of the nuclear masses but also through the influence of the masses on β-decay and neutron capture rates. We point out the importance of the nonequilibrium end stage of the *r* process in determining the width of the resulting abundance pattern uncertainty bands. We additionally make the first identifications of specific parameters of Skyrme-like energy density functionals which show tentative correlations with particular aspects of the *r*-process abundance pattern. While previous studies have explored the reduction in the abundance pattern uncertainties due to anticipated new measurements of neutron-rich nuclei, here we point out that an even larger reduction will occur when these new measurements are used to reduce the uncertainty of model predictions of masses, which are then propagated through to the abundance pattern. We make a quantitative prediction for how large this reduction will be.

DOI: 10.1103/PhysRevC.101.055803

I. INTRODUCTION

The heaviest elements owe their origins to rapid neutron capture, or *r* process, nucleosynthesis. In the *r* process, heavy elements are built up via a sequence of rapid neutron captures and β decays that populate nuclei far to the neutron-rich side of stability [1,2]. The astrophysical source of the intense neutron flux was initially suspected to be within core-collapse supernovae [3,4], though decades of careful study have shown the required conditions are unlikely to be obtained in this environment [5–8]. Recent evidence [9,10], including the dramatic discovery of GW170817/GRB170817a/SSS17a [11,12], increasingly points to neutron star mergers as the likely *r*-process site. However, many open questions remain. For example, what specific environments within neutron star merger events are responsible for *r*-process production, and what are their properties? Can neutron star mergers account for all galactic *r*-process production, or are there additional astrophysical sites?

The *r*-process astrophysical conditions could in principle be identified by comparing simulations of abundance patterns of elements and observations in the solar system and in old stars. However, analysis of individual environments is complicated by large uncertainties in the astrophysics and nuclear physics [13]. Here, we consider the latter. Simulations of the *r* process are dependent upon nuclear data, including masses, neutron capture rates, and β-decay and fission properties, for thousands of neutron-rich nuclei [14]. In spite of a concerted effort at radioactive beam facilities worldwide to measure these properties directly or indirectly, the vast majority of them are as of yet inaccessible and we must rely on theoretical estimates.

Nuclear density functional theory (DFT) is currently the only approach that can provide all of these properties in a consistent yet microscopic framework [15]. However, most energy density functionals (EDF) are phenomenological and lack a rigorous connection with the modern theory of nuclear forces. They are typically characterized by approximately a dozen parameters that are fitted on a small set of nuclear properties. The choices made in selecting the form of the EDF and the set of experimental data to fit its parameters lead to both systematic and statistical uncertainties that have an impact on all applications [16].

Ideally, one would like to consider simultaneously all sources of uncertainties (systematic, statistical and numerical) and propagate them to all observables (separation energies, α-, β- and γ-decay rates, fission rates, neutron capture rates) relevant to astrophysical simulations. Such an approach is currently not feasible, partly because of its formidable computational cost, partly because there are still gaps in our understanding of, e.g., α decay, neutron capture, or fission. However, we can exploit recent work in determining

estimates of theoretical uncertainties to quantify the variations in simulated *r*-process abundances that result from nuclear mass uncertainties alone. Past work in this area has either considered abundance pattern comparisons between distinct mass models to probe model and systematic uncertainties, e.g., [17], or ranges of patterns that result from random, uncorrelated mass variations to estimate aggregate uncertainties of all types [14,18].

In this work, we perform the first rigorous propagation of statistical uncertainties of nuclear mass models based on DFT. In Sec. II, we generate 50 different EDFs by sampling the Bayesian posterior distribution of the UNEDF1 EDF. Continuing in Sec. III, we compute a full nuclear chart and update neutron capture rates and β-decay properties to be consistent with each table. We implement these sets of nuclear data in *r*-process simulations to place "error bars" due to nuclear masses on *r*-process abundances and to identify correlations between theoretical model parameters and abundance pattern features. Such correlations could possibly lead to additional constraints on *r*-process conditions or, e.g., the UNEDF1 parameters themselves. Finally, we provide a quantitative estimate of the improvements to *r*-process pattern uncertainties expected from anticipated mass measurements at current and upcoming facilities and concurrent advancements in theoretical models.

II. MASS TABLE CALCULATIONS

We begin by computing atomic mass tables within the nuclear DFT approach to nuclear structure with Skyrme EDFs. Our starting point is the UNEDF1 parametrization, in which the coupling constants were optimized globally on select experimental nuclear masses, radii, deformations, and excitation energies of fission isomers in the actinides [19]. While the rms deviation on nuclear binding energies of UNEDF1 is 1.8 MeV, it goes down to 0.45 MeV for two-neutron separation energies. Bayesian inference methods were later used to compute the posterior distribution of the UNEDF1 parameters [20] and propagate theoretical statistical uncertainties in predictions of nuclear masses, two-neutron drip line, and fission barriers [21]. Here, we sample the same posterior distribution within the 90% confidence region to generate 50 different parameter sets for the Skyrme EDF.

For each sample, we compute the nuclear ground-state binding energy $B(Z, N)$ of all even-even nuclei from hydrogen to $Z = 120$ by solving the Hartree-Fock-Bogoliubov (HFB) equation. The limits of nuclear stability (proton and neutron drip lines) are reached when the value of the two neutron (proton) separation energy becomes negative. Compared to alternative options based, e.g., on the value of the Fermi energy, this criterion offers the advantage of being model-independent since binding energies are true observables. With this criterion, each mass table contains of the order of 2000 even-even nuclei. For each even-even nucleus, the ground-state is determined by exploring locally the potential energy surface of the nucleus for a range of eleven axial quadrupole deformations β_2 between -0.5 and $+0.5$. The configuration with the lowest energy defines the ground state. Details of the exploration of the even-even nuclear landscape with the numerical solver HFBTHO can be found in [22]. With this procedure, computing 50 mass tables requires of the order of 10^6 HFB calculations.

Although odd-even and odd-odd binding energies could be computed with the blocking procedure, see, e.g., [23], this would require about an order of magnitude more HFB calculations. Instead we adopt a standard approximation for the binding energy of odd nuclei that combines information about binding energies and HFB pairing gaps in neighboring isotopes/isotones; see the Supplemental Material of [24]. This procedure yields an excellent approximation of, in particular, one-particle separation energies.

III. NUCLEOSYNTHESIS CALCULATIONS

For each of the 50 mass tables thus described, we calculate a set of all nuclear data inputs required for *r*-process calculations. We calculate neutron capture and neutron-induced fission rates using the Los Alamos Hauser-Feshbach code COH [25] and β-decay half-lives with probabilities for delayed emission of one or more neutrons using the QRPA + HF framework of [26] and unmodified strength data from [27]. We repeat these calculations using the masses given in the 2016 Atomic Mass Evaluation [28]; where these calculations are possible, the results are taken to replace those based on the UNEDF1 mass tables. The decay properties of the NUBASE 2016 compilation [29] are further taken to replace any calculated values based on either AME2016 or UNEDF1 nuclear masses. For all fissioning nuclei, we use a symmetric, two-particle product distribution.

It is important to note that in all of our theoretical calculations, there are additional dependencies beyond nuclear masses alone, including γ and β strength functions and nuclear level densities. It is unfortunately well beyond current capabilities to calculate these inputs for each of the 50 UNEDF1 parametrizations. We emphasize that the purpose of the present work is to examine *r*-process uncertainties that result from the statistical uncertainties in the UNEDF1 nuclear masses only as they enter directly into these calculations, with all other dependencies held fixed.

We implement each of these data sets into the nuclear reaction network code PRISM [30–32] to simulate nucleosynthesis for three distinct types of astrophysical conditions where *r*-process nucleosynthesis may occur: (1) a supernova-type high-entropy wind, with entropy $s/k = 300$, dynamical timescale $\tau = 80$ ms, and electron fraction $Y_e = 0.30$, (2) a parametrized merger accretion disk wind with $s/k = 30$, $\tau = 80$ ms, and $Y_e = 0.21$, and (3) fission-recycling outflow from a neutron star merger [33]. For each simulation, we dynamically update the evolution of temperature with respect to the release of energy from nuclear reactions, decays, and fission, with an assumed thermalization efficiency of 10% for all energy released. The release of energy is calculated using the masses of AME2016 where applicable and the corresponding UNEDF1 mass table elsewhere.

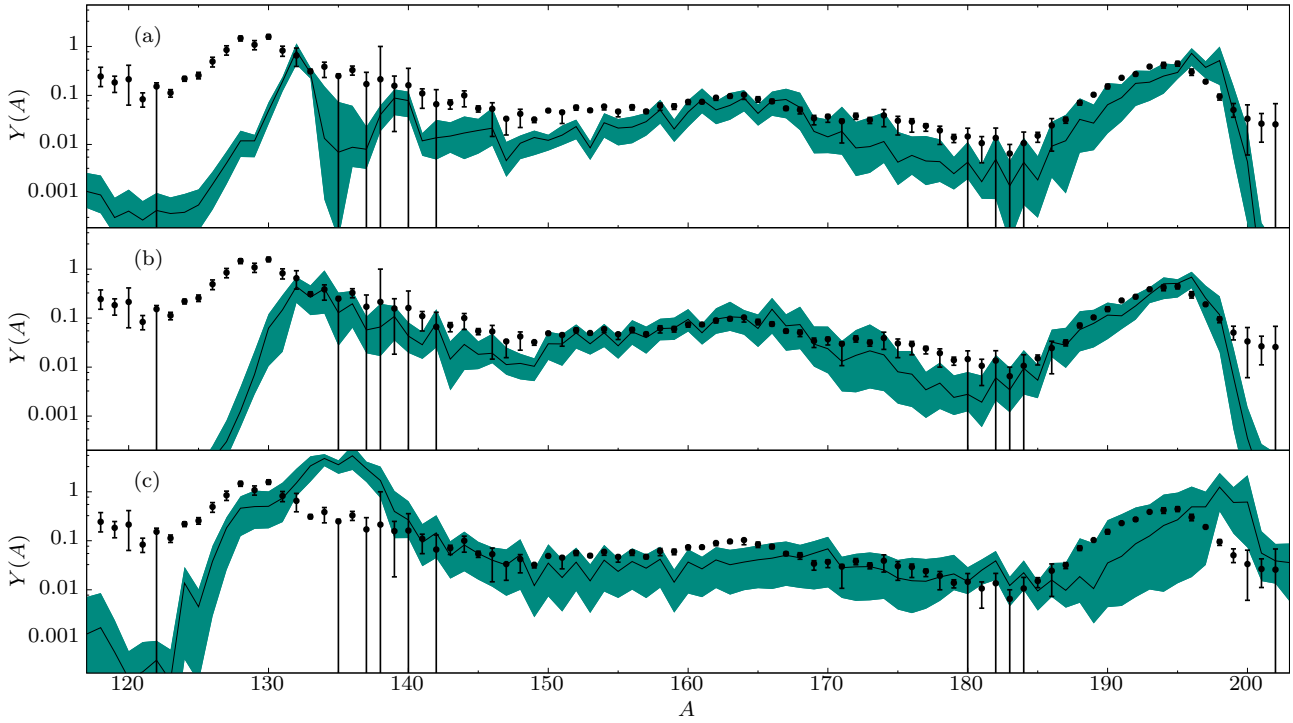

FIG. 1. Abundance patterns $Y(A)$ versus A for 50 r-process simulations with astrophysical conditions corresponding to high-entropy (a), low-entropy (b), and fission-recycling (c) outflows, as described in the text. The shaded region shows the full range of abundance patterns produced, and the black line shows their mean. All patterns are scaled to solar abundances from [13].

A. Propagation of statistical uncertainties to *r*-process nucleosynthesis

The range in abundance patterns across the 50 UNEDF1 mass tables with experimental nuclear data is shown for each of these three conditions in Fig. 1. The calculations corresponding to the nominal UNEDF1 table are scaled to the solar data of [13]; these scale factors are applied uniformly to each of the 50 calculations in determining the presented ranges. Furthermore, we note that the abundance pattern variations converged in all cases after the consideration of ≈35 UNEDF1 mass tables, with this convergence holding across all 50 tables, as demonstrated in Fig. 2. There nevertheless remains the possibility that these ranges may change under the consideration of substantially more samplings within the UNEDF1 parameter space.

The varying widths of the r-process abundance ranges reflect the role of nuclear masses in shaping the abundance patterns in each type of astrophysical conditions. In each case, nucleosynthesis initially proceeds through a long (n,γ)-(γ,n) equilibrium phase, where we observe the abundances along each isotopic chain to follow a Saha equation,

$$\frac{Y(Z,N+1)}{Y(Z,N)} \propto \frac{G(Z,N+1)}{2G(Z,N)} \frac{N_n}{(kT)^{3/2}} e^{\frac{S_n(Z,N+1)}{kT}}, \qquad (1)$$

where $G(Z,N)$ are the partition functions, N_n is the neutron number density, kT is the temperature in MeV, and $S_n(Z,N+1)$ are the neutron separation energies. During this phase of nucleosynthesis, the primary source of variations between the 50 calculations arise from the different one-neutron separation energies predicted by each mass table as they enter into Eq. (1).

For both wind conditions, the breakdown of (n,γ)-(γ,n) equilibrium is mediated by the exhaustion of free neutrons, and the competition between β decay, neutron capture, and

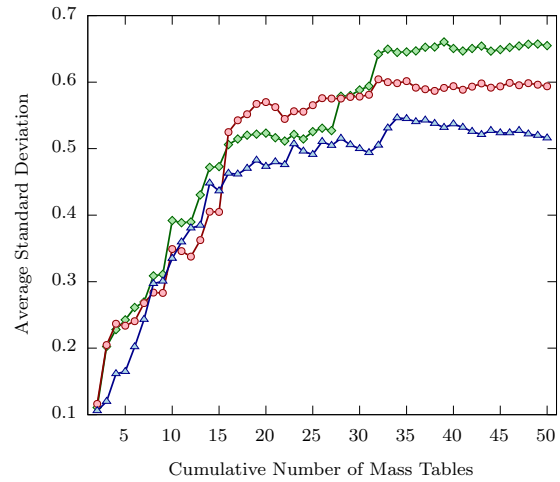

FIG. 2. Average standard deviation of calculated nuclear abundances as a function of cumulative number of UNEDF1 mass tables considered in this work. Abundance pattern variations begin to converge once the first ≈35 mass tables are considered for each of the high-entropy (green diamonds), low-entropy (red circles), and fission recycling (blue triangles) conditions from Fig. 1. Convergence holds as the number of UNEDF1 mass tables is extended to 50.

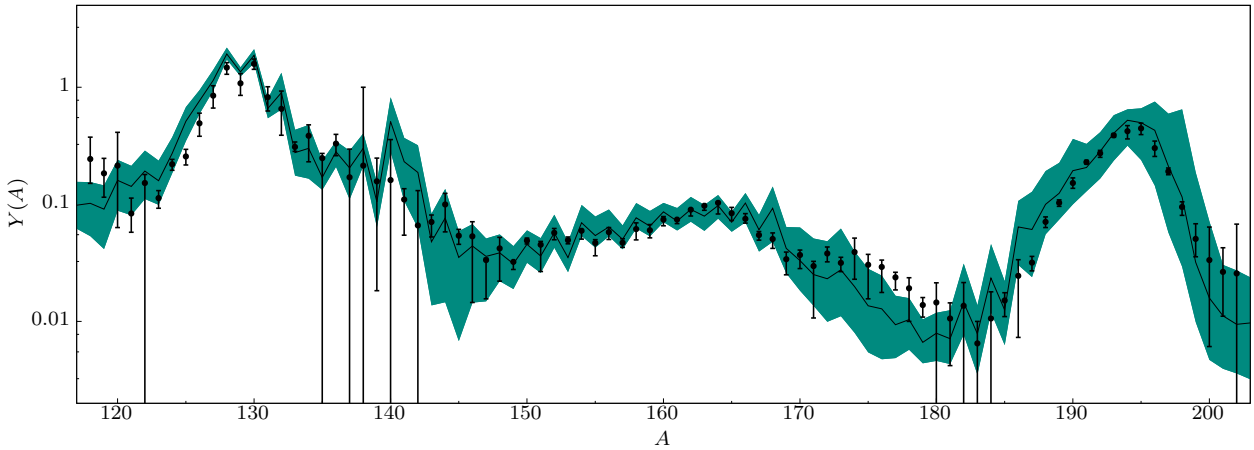

FIG. 3. Total abundance patterns $Y(A)$ vs A for 50 r-process simulations based on the simulated disk ejecta conditions of [34]. The shaded region corresponds to the total range of abundance patterns and the black line to their mean, as in Fig. 1.

photodissociation dictates the final abundance pattern. Of these processes, photodissociation rates have the strongest dependence on nuclear masses. Consequently, variations between the 50 mass tables propagate to variations in calculated abundance patterns primarily through different photodissociation rates.

For the fission recycling example, the (n,γ)-(γ,n) equilibrium path for nucleosynthesis follows the one-neutron drip line, the location of which can vary by more than ten neutron numbers across the 50 mass tables, with the most prominent differences located near the $N = 184$ shell closure. We find the drip line variations to dominate any variations among late-time photodissociation rates in determining the width of the calculated abundance patterns in this case, with an overall width that is approximately twice that of either of the wind conditions we consider.

In the context of a complete astrophysical r-process event, the overall abundance pattern will be the sum total of material produced in a range of individual environments, with distributions in electron fraction, entropy, and final velocity expected for ejected material. By sampling conditions that represent distinct regimes for the r process, these results give a general estimate of uncertainty that can be expected in a more complete model of nucleosynthesis in an astrophysical r-process event. For such a model, the total nuclear uncertainty of the type considered here is approximately a linear combination of those shown in Fig. 1. In order to demonstrate this effect, we examine the nucleosynthesis of a neutron star-neutron star merger event by considering the M3A8m03a2 disk ejecta simulation of [34]. We calculate the full mass-weighted abundance pattern for this simulation using the nominal UNEDF1 data set and identify a subset of ten trajectories whose summed abundances reproduce the mass-weighted pattern. For each of these ten trajectories, we perform nucleosynthesis calculations using the 50 UNEDF1 mass tables and present the corresponding range in Fig. 3. The overall width is comparable to those shown in the three panels of Fig. 1.

B. Correlations between UNEDF1 parameters and r-process features

With the wealth of data available from the r-process simulations shown in Fig. 1, we can search for correlations between UNEDF1 functional parameters and the formation of abundance pattern features. In the absence of all other uncertainties entering into r-process simulations, these correlations could provide important constraints on r-process nucleosynthesis and certain UNEDF1 parameters. While this is not presently the case, we demonstrate here how such an analysis may proceed. As astrophysical and nuclear models continue to improve, the general method demonstrated here may prove useful. Important requirements for such future work would include the consideration of many more sample points within a nuclear EDF model's parameter space in order to develop a more robust understanding of these correlations' statistics, as well as a more comprehensive implementation of nuclear model predictions in the calculation of capture, decay, and fission properties relevant to the r process, as discussed at the end of Sec. III.

Several of the UNEDF1 functional parameters are poorly constrained by data near stability. One such parameter is the isovector surface coupling constant $C_1^{\rho\Delta\rho}$, with UNEDF1 value -145.382 ± 52.169; see Table II in [19]. For a low-entropy hot wind r-process environment, this parameter is correlated with the formation of the rare earth peak, the small feature around $A \sim 160$ in the solar r-process isotopic pattern. In particular, we consider the abundance-weighted average A of the rare earth peak, given by

$$\left(\sum_{150\leqslant A\leqslant 175} A \times Y(A)\right) \Big/ \left(\sum_{150\leqslant A\leqslant 175} Y(A)\right). \qquad (2)$$

The top panel of Fig. 4 shows $C_1^{\rho\Delta\rho}$ versus the abundance-weighted average A of the rare earth peak for the r-process simulations from the middle panel of Fig. 1. The placement of the rare earth peak is calculated from the solar r-process

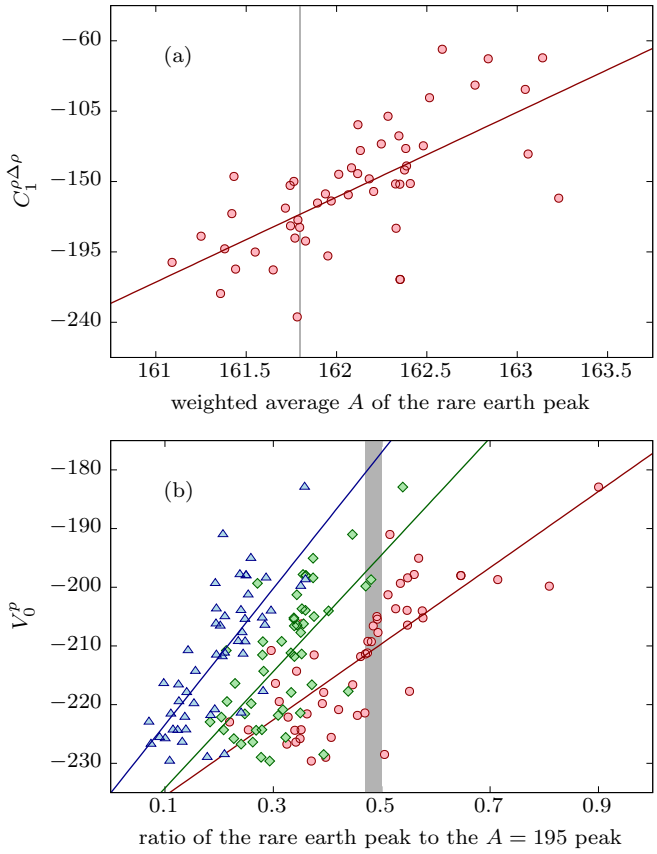

FIG. 4. Relationship between r-process abundance pattern and UNEDF1 functional parameters for 50 UNEDF1 mass tables. (a) shows the relationship between the weighted average mass number A of the rare earth peak and the isovector surface coupling constant $C_1^{\rho\Delta\rho}$ for the low-entropy wind conditions of Fig. 1. A linear fit to the data set is given by the solid line with correlation coefficient $r = 0.68$. (b) shows the relationship between the proton pairing strength V_0^p and the ratio of summed abundances in the rare earth region to the $A = 195$ region for the high-entropy (green diamonds), low-entropy (red circles), and fission recycling (blue triangles) conditions from Fig. 1, with linear fits given for the high-entropy data set by the green dashed line ($r = 0.66$), the low-entropy data set by the red solid line ($r = 0.76$), and the fission recycling data set by the blue dot-dashed line ($r = 0.75$). The gray shaded region in each figure indicates the range of values in each metric admitted by the solar abundances of [13,35].

abundances of [13,35] and is given by the shaded vertical band. Correlations between $C_1^{\rho\Delta\rho}$ and rare earth peak placement are weaker for other types of r-process environments. The r-process path in the high-entropy wind case is not so neutron-rich and thus not as sensitive to $C_1^{\rho\Delta\rho}$. The fission recycling example has a distinct rare earth peak formation mechanism [36] that is not particularly active with the UNEDF1 masses, resulting in a comparatively weaker correlation. However, recent studies [34,37–41] favor r-process conditions that are most similar to those of our low-entropy wind where this correlation is strongest, suggesting that the r-process abundance pattern may provide an important additional constraint on the value of $C_1^{\rho\Delta\rho}$.

In all of the astrophysical environments considered, we also found the proton pairing strength V_0^p to be correlated with the ratio between the summed abundances of the rare earth ($150 \leqslant A \leqslant 175$) and $A \sim 195$ ($185 \leqslant A \leqslant 205$) peak regions, as illustrated in the bottom panel of Fig. 4, where the solar values are again given by the shaded band. The correlations in each case are distinct, with different astrophysical conditions picking out different preferred values of V_0^p. Only the least negative values of V_0^p considered reproduce solar values for the high-entropy conditions, while values of V_0^p that tend towards the center of the distribution reproduce solar values for the low-entropy conditions. Within the range of values we consider for V_0^p, the fission recycling conditions fail to reproduce solar values, with the correlation suggesting an even more negative value of V_0^p. Thus, if V_0^p could be more tightly constrained, the simulated ratio of the rare earth and $A \sim 195$ peak regions could be used as a diagnostic of r-process conditions.

C. Impact of future experimental campaigns on r-process simulations

Measurements of the masses of increasingly neutron-rich nuclei are the focus of a number of experimental efforts worldwide, for example at the Canadian Penning Trap at CARIBU [42,43], JYFLTRAP at Jyväskylä [44,45], ISOLTRAP at CERN [46], TITAN at TRIUMF [47], and storage rings at GSI in Germany, IMP in China, and RIKEN in Japan [48]. Next-generation radioactive ion facilities, such as the Facility for Rare Isotope Beams (FRIB) under construction at Michigan State University, will have unprecedented access to isotopes far from stability [49]. New mass measurements improve the reliability of r-process simulations in two ways: directly, by dramatically reducing the uncertainty in the masses of newly measured nuclei, and indirectly, by enabling improvements to mass modeling. Theoretical mass models are all calibrated in some way with known data, so known masses tend to be well reproduced by theory. Outside the known region, theoretical predictions tend to diverge. The variations among our 50 UNEDF1 mass tables, shown for the tin isotopes in Fig. 5, clearly demonstrate this behavior. For this element, UNEDF1 fits known masses to about $\sigma_{\rm rms} \sim 1$ MeV, and variations increase sharply past the $N = 82$ closed shell.

Additional measurements increase the available data with which to constrain theory and thus hold the potential to reduce uncertainties outside the measured region. We generate an adjusted set of 50 mass tables to capture this effect. For nuclei within the range of the AME2016 compilation, we leave the masses at their original values. Along each isotopic chain and between the respective ranges of AME2016 and FRIB, we reduce the variations among the original 50 tables until the rms deviation from the nominal UNEDF1 table matches that of the most neutron-rich isotope in AME2016. Finally, we contract the variations for nuclei beyond the reach of FRIB until the r.m.s deviation is reduced by a fixed amount, such that the deviation as a function of neutron number runs parallel to that of the original table. The overall effect of this process can be seen by comparing the light green (original tables) and dark green (modified tables) regions in Fig. 5.

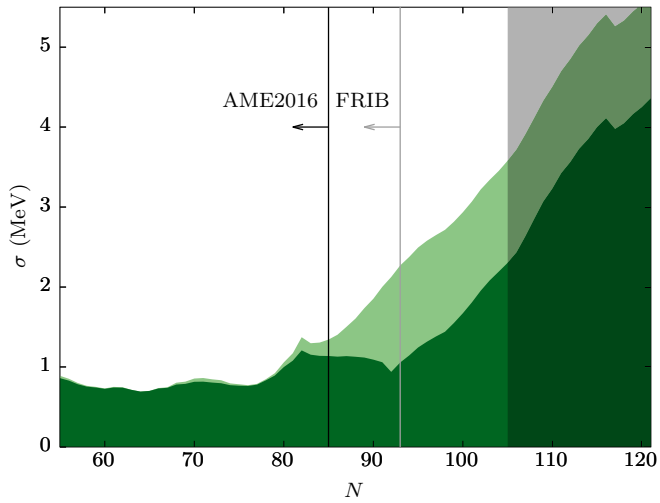

FIG. 5. Variations σ among our set of 50 UNEDF1 mass tables (light green shaded region) and our set of simulated mass tables (dark green shaded region), each with respect to the nominal UNEDF1 masses, for the tin ($Z = 50$) isotopic chain. The AME2016 range of known masses [28] and anticipated FRIB reach are indicated, respectively, by black and gray solid lines. The vertical darkened band ($N = 105 - 121$) indicates the range in location for the one-neutron dripline.

Our two sets of UNEDF1 mass tables can be used to quantify the reductions in r-process abundance pattern uncertainties that have already been achieved by measurements to date and that are anticipated from future mass measurements. We rerun the example r-process simulations from Fig. 1 using three different sets of nuclear data. The first set is a theory-only set, with all quantities derived exclusively from our 50 UNEDF1 tables. The second set is that used in Fig. 1, where experimental nuclear data is additionally incorporated. The third set is constructed to mimic the influence of anticipated mass measurements. Experimental values or values derived from the nominal UNEDF1 mass tables are used (and not varied) for all nuclei within the FRIB reach; elsewhere we use theory values derived from our set of 50 simulated UNEDF1 mass tables.

Figure 6 shows the abundance pattern variations normalized by the mean for the three astrophysical trajectories in Fig. 1, each calculated with the three data sets described above. To provide a comparison of the statistical uncertainties considered in this work with model uncertainty, we additionally include the variations across calculations based on fifteen distinct mass models, indicated by the lightest-shaded gray region in this figure.

For the high entropy wind case, Fig. 6(a), many of the nuclear properties important for the freeze-out phase have already been measured, so there is significant improvement realized between the theory-only (lightest shaded band) calculations and those that include current experimental values (medium shaded band). Looking forward to FRIB, the majority of nuclei along the equilibrium r-process path in the $N = 82$ and rare earth regions will be within reach. Thus

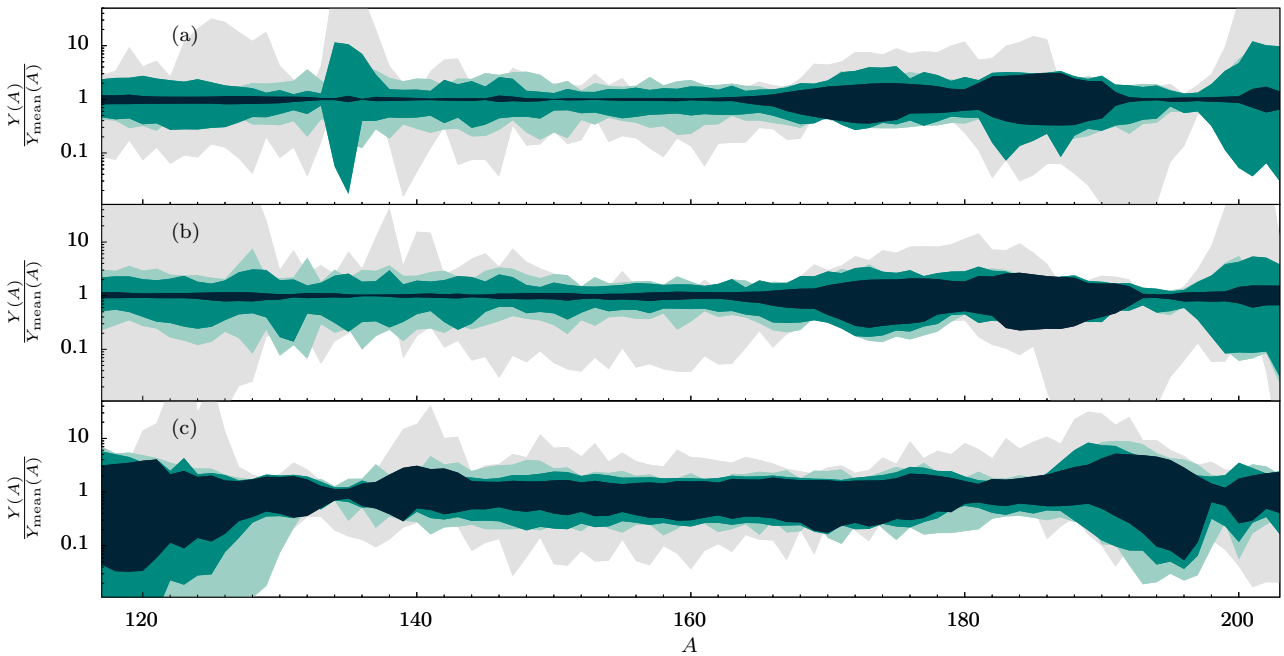

FIG. 6. Ratios of the abundances $Y(A)$ to the mean abundance $Y_{\text{mean}}(A)$ for the set of 50 simulations with the example high entropy wind (a), low entropy wind (b), and fission recycling outflow (c) astrophysical conditions, as in Fig. 1. The light shaded band shows theory-only calculations, the medium shaded band implements AME2016 masses and NUBASE2016 decay properties where available, and the dark shaded band additionally includes the simulated mass tables described in the text. The lightest-shaded grey region shows the analogous range for a set of 15 distinct, non-UNEDF1 mass tables (FRDM1995 [50], FRDM2012 [51], Duflo-Zuker [52], ETFSI [53], ETFSI-q [54],Thomas-Fermi [55], Weizsäcker-Skyrme (WS) [56,57], KTUY05 [58], HFB21 [59], HFB22 [60], SkM* [61], SkP [62], SLy4 [63], SV-min [64], and UNEDF0 [65]).

systematic measurement campaigns at FRIB have the potential to essentially remove mass as a source of uncertainty in simulated r-process abundances below $A \sim 170$ for high entropy winds.

High entropy winds, however, are unlikely to be obtained in the currently favored potential r-process astrophysical site of neutron star/neutron star-black hole mergers. Here, the environments are likely lower entropy, $s/k \sim 5$–50, and more neutron-rich, similar to the conditions used for the middle and bottom panels of Figs. 1 and 6. The r-process equilibrium paths are farther from stability in these cases, thus the current reach of experimental data results in more modest improvements, as indicated when comparing the light- and medium-shaded bands in Fig. 6(b) and 6(c). Prospects for the future, however, are encouraging. For the low-entropy wind example of Fig. 6(b), FRIB can reach the majority of the key nuclei and the remaining uncertainty band should be similar to the high-entropy wind case. In particular the excellent precision anticipated for abundances $140 < A < 170$ can facilitate the use of the rare earth peak as a key r-process diagnostic [43,66].

For the fission recycling example, uncertainties in the location of the drip line and in the fission properties of heavy nuclei near the drip line dominate the uncertainty bands. Even with FRIB at full power these uncertainties are unlikely to be resolved with direct measurements. Here, nuclear theory will play a critical role. The simulated improvements to theory anticipated in our approach do result in a narrowing of the uncertainty band, as seen in a comparison between the medium- and dark-shaded bands of Fig. 6(c). Further potential improvements to nuclear EDF theory, e.g., [67], and its full application to the problem of fission, e.g., [68,69], are not captured in our approach. Therefore, there remains the possibility for more significant improvements to the uncertainty band associated with fission-recycling conditions with concurrent advances in experiment and theory.

IV. SUMMARY

In this work, we investigate the influence of statistical uncertainty associated with one Skyrme energy density functional, UNEDF1, on r-process nucleosynthesis simulations. We calculate mass tables for 50 parameter sets within the 90% confidence region of UNEDF1. For each of these tables, we calculate one-neutron separation energies, neutron capture rates, and β-decay properties based on the table's associated Q values. We note the importance of future work that implements additional nuclear structure predictions arising from nuclear EDFs in these calculations.

We perform nucleosynthesis simulations based on each set of data for three distinct r-process conditions and demonstrate that the nuclear uncertainties associated with the total nucleosynthesis of a neutron star-neutron star merger is broadly consistent with that of the individual conditions we consider.

By considering r-process abundances as a function of the UNEDF1 parameters, we identify potential correlations between r-process abundance features and the isovector surface coupling and proton pairing strength parameters. We comment on how such correlations may be used in the future to provide additional constraints on nuclear EDFs. We identify as possible future work additional steps that are needed to better understand the correlations hinted in this work, including a more comprehensive inclusion of points within a nuclear EDF's parameter space and a more robust implementation of nuclear model predictions in the calculation of nuclear properties relevant to the r process.

Finally, we anticipate the ability of future experiments at FRIB to further constrain the UNEDF1 EDF and evaluate the resulting improvements to r-process abundance uncertainties. We show that future FRIB experiments may substantially improve r-process simulations in low-entropy and high-entropy wind environments, with more modest improvements expected for fission-recycling conditions.

ACKNOWLEDGMENTS

This work was supported in part by the US Department of Energy under Grants No. DE-SC0013039 (R.S.), No. DE-FG02-95-ER40934 (R.S.), No. DE-FG02-02ER41216 (G.C.M.), and No. DE-FG02-93ER-40756 (R.N.P.), and the SciDAC collaborations TEAMS DE-SC0018232 (T.M.S., R.S.) and NUCLEI DE-SC0018223 (R.N.P., N.S.). Part of this work was carried out under the auspices of the National Nuclear Security Administration of the US Department of Energy at Los Alamos National Laboratory under Contract No. 89233218CNA000001 (T.M.S., M.R.M.); under the auspices of the US Department of Energy by Lawrence Livermore National Laboratory under Contract No. DE-AC52-07NA27344 (N.S.); under the FIRE topical collaboration in nuclear theory funded by the US Department of Energy under Contract No. DE-AC52-07NA27344 (R.S., M.R.M., G.C.M.). This work was also supported in part by Los Alamos National Laboratory (LANL) through its Center for Space and Earth Science (CSES). CSES is funded by LANL's Laboratory Directed Research and Development (LDRD) program under Project No. 20180475DR (T.M.S.). Computing support for this work came from the Lawrence Livermore National Laboratory (LLNL) Institutional Computing Grand Challenge program.

[1] E. M. Burbidge, G. R. Burbidge, W. A. Fowler, and F. Hoyle, Synthesis of the elements in stars, Rev. Mod. Phys. **29**, 547 (1957).

[2] A. G. W. Cameron, Nuclear Reactions in Stars and Nucleogenesis, Chalk River Reports, CRL-41, 1957.

[3] B. S. Meyer, G. J. Mathews, W. M. Howard, S. E. Woosley, and R. D. Hoffman, R-process nucleosynthesis in the high-entropy supernova bubble, Astrophys. J. **399**, 656 (1992).

[4] S. E. Woosley, J. R. Wilson, G. J. Mathews, R. D. Hoffman, and B. S. Meyer, The r-process and neutrino-heated supernova ejecta, Astrophys. J. **433**, 229 (1994).

[5] A. Arcones, H.-T. Janka, and L. Scheck, Nucleosynthesis-relevant conditions in neutrino-driven supernova outflows. I. Spherically symmetric hydrodynamic simulations, Astron. Astrophys. **467**, 1227 (2007).

[6] T. Fischer, S. C. Whitehouse, A. Mezzacappa, F.-K. Thielemann, and M. Liebendörfer, Protoneutron star evolution and the neutrino-driven wind in general relativistic neutrino radiation hydrodynamics simulations, Astron. Astrophys. **517**, A80 (2010).

[7] L. Hüdepohl, B. Müller, H.-T. Janka, A. Marek, and G. G. Raffelt, Neutrino Signal of Electron-Capture Supernovae from Core Collapse to Cooling, Phys. Rev. Lett. **104**, 251101 (2010).

[8] L. F. Roberts, S. Reddy, and G. Shen, Medium modification of the charged-current neutrino opacity and its implications, Phys. Rev. C **86**, 065803 (2012).

[9] Y. Hirai, Y. Ishimaru, T. R. Saitoh, M. S. Fujii, J. Hidaka, and T. Kajino, Enrichment of r-process elements in dwarf spheroidal galaxies in chemo-dynamical evolution model, Astrophys. J. **814**, 41 (2015).

[10] A. P. Ji, A. Frebel, A. Chiti, and J. D. Simon, R-process enrichment from a single event in an ancient dwarf galaxy, Nature **531**, 610 (2016).

[11] B. P. Abbott *et al.*, Gw170817: Observation of Gravitational Waves from a Binary Neutron Star Inspiral, Phys. Rev. Lett. **119**, 161101 (2017).

[12] P. S. Cowperthwaite *et al.*, The electromagnetic counterpart of the binary neutron star merger ligo/virgo gw170817. ii. uv, optical, and near-infrared light curves and comparison to kilonova models, Astrophys. J. Lett. **848**, L17 (2017).

[13] M. Arnould, S. Goriely, and K. Takahashi, The r-process of stellar nucleosynthesis: Astrophysics and nuclear physics achievements and mysteries, Phys. Rep. **450**, 97 (2007).

[14] M. R. Mumpower, R. Surman, G. C. McLaughlin, and A. Aprahamian, The impact of individual nuclear properties on r-process nucleosynthesis, Prog. Part. Nucl. Phys. **86**, 86 (2016).

[15] M. Bender, P.-H. Heenen, and P.-G. Reinhard, Self-consistent mean-field models for nuclear structure, Rev. Mod. Phys. **75**, 121 (2003).

[16] N. Schunck, J. D. McDonnell, D. Higdon, J. Sarich, and S. M. Wild, Uncertainty quantification and propagation in nuclear density functional theory, Eur. Phys. J. A **51**, 169 (2015).

[17] D. Martin, A. Arcones, W. Nazarewicz, and E. Olsen, Impact of Nuclear Mass Uncertainties on the r Process, Phys. Rev. Lett. **116**, 121101 (2016).

[18] R. Surman, M. Mumpower, and A. Aprahamian, Uncorrelated nuclear mass uncertainties and r-process abundance predictions, Acta Phys. Pol. B **47**, 673 (2016).

[19] M. Kortelainen, J. McDonnell, W. Nazarewicz, P. G. Reinhard, J. Sarich, N. Schunck, M. V. Stoitsov, and S. M. Wild, Nuclear energy density optimization: Large deformations, Phys. Rev. C **85**, 024304 (2012).

[20] D. Higdon, J. D. McDonnell, N. Schunck, J. Sarich, and S. M. Wild, A Bayesian approach for parameter estimation and prediction using a computationally intensive model, J. Phys. G **42**, 034009 (2015).

[21] J. D. McDonnell, N. Schunck, D. Higdon, J. Sarich, S. M. Wild, and W. Nazarewicz, Uncertainty Quantification for Nuclear Density Functional Theory and Information Content of New Measurements, Phys. Rev. Lett. **114**, 122501 (2015).

[22] R. Navarro Perez, N. Schunck, R. D. Lasseri, C. Zhang, and J. Sarich, Axially deformed solution of the Skyrme–Hartree–Fock–Bogolyubov equations using the transformed harmonic oscillator basis (III) HFBTHO (v3.00): A new version of the program, Comput. Phys. Commun. **220**, 363 (2017).

[23] N. Schunck, J. Dobaczewski, J. McDonnell, J. Moré, W. Nazarewicz, J. Sarich, and M. V. Stoitsov, One-quasiparticle states in the nuclear energy density functional theory, Phys. Rev. C **81**, 024316 (2010).

[24] J. Erler, N. Birge, M. Kortelainen, W. Nazarewicz, E. Olsen, A. M. Perhac, and M. Stoitsov, The limits of the nuclear landscape, Nature **486**, 509 (2012).

[25] T. Kawano, R. Capote, S. Hilaire, and P. Chau Huu-Tai, Statistical Hauser-Feshbach theory with width-fluctuation correction including direct reaction channels for neutron-induced reactions at low energies, Phys. Rev. C **94**, 014612 (2016).

[26] M. R. Mumpower, T. Kawano, and P. Möller, Neutron-γ competition for β-delayed neutron emission, Phys. Rev. C **94**, 064317 (2016).

[27] P. Möller, J. R. Nix, and K. L. Kratz, Nuclear properties for astrophysical and radioactive-ion beam applications, At. Data Nucl. Data Tables **66**, 131 (1997).

[28] M. Wang, G. Audi, F. G. Kondev, W. J. Huang, S. Naimi, and Xing Xu, The AME2016 atomic mass evaluation (II). Tables, graphs and references, Chin. Phys. C **41**, 030003 (2017).

[29] G. Audi *et al.*, The nubase2016 evaluation of nuclear properties, Chin. Phys. C **41**, 030001 (2017).

[30] M. R. Mumpower, T. Kawano, J. L. Ullmann, M. Krtika, and T. M. Sprouse, Estimation of M 1 scissors mode strength for deformed nuclei in the medium- to heavy-mass region by statistical Hauser-Feshbach model calculations, Phys. Rev. C **96**, 024612 (2017).

[31] M. R. Mumpower, T. Kawano, T. M. Sprouse, N. Vassh, E. M. Holmbeck, R. Surman, and P. Möller, β-delayed fission in r-process nucleosynthesis, Astrophys. J. **869**, 14 (2018).

[32] E. M. Holmbeck, T. M. Sprouse, M. R. Mumpower, N. Vassh, R. Surman, T. C. Beers, and T. Kawano, Actinide production in the neutron-rich ejecta of a neutron star merger, Astrophys. J. **870**, 23 (2018).

[33] J. de Jesús Mendoza-Temis, M.-R. Wu, K. Langanke, G. Martínez-Pinedo, A. Bauswein, and H.-T. Janka, Nuclear robustness of the *r* process in neutron-star mergers, Phys. Rev. C **92**, 055805 (2015).

[34] O. Just, A. Bauswein, R. Ardevol Pulpillo, S. Goriely, and H.-T. Janka, Comprehensive nucleosynthesis analysis for ejecta of compact binary mergers, Mon. Not. R. Astron. Soc. **448**, 541 (2015).

[35] C. Sneden, J. J. Cowan, and R. Gallino, Neutron-capture elements in the early galaxy, Annu. Rev. Astron. Astrophys. **46**, 241 (2008).

[36] M. R. Mumpower, G. C. McLaughlin, R. Surman, and A. W. Steiner, Reverse engineering nuclear properties from rare earth abundances in the r process, J. Phys. G **44**, 034003 (2017).

[37] G. C. McLaughlin and R. Surman, Prospects for obtaining an r process from gamma ray burst disk winds, Nucl. Phys. A **758**, 189 (2005).

[38] R. Surman, G. C. McLaughlin, and W. R. Hix, Nucleosynthesis in the outflow from gamma-ray burst accretion disks, Astrophys. J. **643**, 1057 (2006).

[39] D. Martin, A. Perego, A. Arcones, F.-K. Thielemann, O. Korobkin, and S. Rosswog, Neutrino-driven winds in the aftermath of a neutron star merger: Nucleosynthesis and electromagnetic transients, Astrophys. J. **813**, 2 (2015).

[40] S. Wanajo, Y. Sekiguchi, N. Nishimura, K. Kiuchi, K. Kyutoku, and M. Shibata, Production of all the r-process nuclides in the

dynamical ejecta of neutron star mergers, Astrophys. J. Lett. **789**, L39 (2014).

[41] D. M. Siegel and B. D. Metzger, Three-Dimensional General-Relativistic Magnetohydrodynamic Simulations of Remnant Accretion Disks from Neutron Star Mergers: Outflows and r-Process Nucleosynthesis, Phys. Rev. Lett. **119**, 231102 (2017).

[42] T. Y. Hirsh, N. Paul, M. Burkey, A. Aprahamian, F. Buchinger, S. Caldwell, J. A. Clark, A. F. Levand, L. L. Ying, S. T. Marley, G. E. Morgan, A. Nystrom, R. Orford, A. P. Galván, J. Rohrer, G. Savard, K. S. Sharma, and K. Siegl, First operation and mass separation with the CARIBU MR-TOF, Nucl. Instrum. Methods Phys. Res. B **376**, 229 (2016).

[43] R. Orford, N. Vassh, J. A. Clark, G. C. McLaughlin, M. R. Mumpower, G. Savard, R. Surman, A. Aprahamian, F. Buchinger, M. T. Burkey, D. A. Gorelov, T. Y. Hirsh, J. W. Klimes, G. E. Morgan, A. Nystrom, and K. S. Sharma, Precision Mass Measurements of Neutron-Rich Neodymium and Samarium Isotopes and Their Role in Understanding Rare-Earth Peak Formation, Phys. Rev. Lett. **120**, 262702 (2018).

[44] A. Kankainen, J. Hakala, T. Eronen, D. Gorelov, A. Jokinen, V. S. Kolhinen, I. D. Moore, H. Penttilä, S. Rinta-Antila, J. Rissanen, A. Saastamoinen, V. Sonnenschein, and J. Äystö, Isomeric states close to doubly magic ^{132}Sn studied with the double Penning trap JYFLTRAP, Phys. Rev. C **87**, 024307 (2013).

[45] M. Vilen, J. M. Kelly, A. Kankainen, M. Brodeur, A. Aprahamian, L. Canete, T. Eronen, A. Jokinen, T. Kuta, I. D. Moore, M. R. Mumpower, D. A. Nesterenko, H. Penttilä, I. Pohjalainen, W. S. Porter, S. Rinta-Antila, R. Surman, A. Voss, and J. Äystö, Precision Mass Measurements on Neutron-Rich Rare-Earth Isotopes at JYFLTRAP: Reduced Neutron Pairing and Implications for r-Process Calculations, Phys. Rev. Lett. **120**, 262701 (2018).

[46] D. Lunney (on behalf of ISOLTRAP Collaboration), Extending and refining the nuclear mass surface with ISOLTRAP, J. Phys. G **44**, 064008 (2017).

[47] D. Lascar, R. Klawitter, C. Babcock, E. Leistenschneider, S. R. Stroberg, B. R. Barquest, A. Finlay, M. Foster, A. T. Gallant, P. Hunt, J. Kelly, B. Kootte, Y. Lan, S. F. Paul, M. L. Phan, M. P. Reiter, B. Schultz, D. Short, J. Simonis, C. Andreoiu, M. Brodeur, I. Dillmann, G. Gwinner, J. D. Holt, A. A. Kwiatkowski, K. G. Leach, and J. Dilling, Precision mass measurements of $^{125-127}$Cd isotopes and isomers approaching the $N = 82$ closed shell, Phys. Rev. C **96**, 044323 (2017).

[48] Y. H. Zhang, Y. A. Litvinov, T. Uesaka, and H. S. Xu, Storage ring mass spectrometry for nuclear structure and astrophysics research, Phys. Scr. **91**, 073002 (2016).

[49] https://groups.nscl.msu.edu/frib/rates/fribrates.html.

[50] P. Moller, J. R. Nix, W. D. Myers, and W. J. Swiatecki, Nuclear ground-state masses and deformations, At. Data Nucl. Data Tables **59**, 185 (1995).

[51] P. Möller, A. J. Sierk, T. Ichikawa, and H. Sagawa, Nuclear ground-state masses and deformations: FRDM (2012), At. Data Nucl. Data Tables **109–110**, 1 (2016).

[52] J. Duflo and A. P. Zuker, Microscopic mass formulas, Phys. Rev. C **52**, R23 (1995).

[53] Y. Aboussir, J. M. Pearson, A. K. Dutta, and F. Tondeur, Nuclear mass formula via an approximation to the Hartree-Fock method, At. Data Nucl. Data Tables **61**, 127 (1995).

[54] J. M. Pearson, R. C. Nayak, and S. Goriely, Nuclear mass formula with Bogolyubov-enhanced shell-quenching: Application to r-process, Phys. Lett. B **387**, 455 (1996).

[55] W. D. Myers and W. J. Swiatecki, Nuclear properties according to the Thomas-Fermi model, Nucl. Phys. A **601**, 141 (1996).

[56] M. Liu, N. Wang, Y. Deng, and X. Wu, Further improvements on a global nuclear mass model, Phys. Rev. C **84**, 014333 (2011).

[57] H. Zhang, J. Dong, N. Ma, G. Royer, J. Li, and H. Zhang, An improved nuclear mass formula with a unified prescription for the shell and pairing corrections, Nucl. Phys. A **929**, 38 (2014).

[58] H. Koura, T. Tachibana, M. Uno, and M. Yamada, Nuclidic mass formula on a spherical basis with an improved even-odd term, Prog. Theor. Phys. **113**, 305 (2005).

[59] S. Goriely, N. Chamel, and J. M. Pearson, Further explorations of Skyrme-Hartree-Fock-Bogoliubov mass formulas. XII. Stiffness and stability of neutron-star matter, Phys. Rev. C **82**, 035804 (2010).

[60] S. Goriely, N. Chamel, and J. M. Pearson, Further explorations of Skyrme-Hartree-Fock-Bogoliubov mass formulas. XIII. The 2012 atomic mass evaluation and the symmetry coefficient, Phys. Rev. C **88**, 024308 (2013).

[61] J. Bartel, P. Quentin, M. Brack, C. Guet, and H. B. Håkansson, Towards a better parametrisation of Skyrme-like effective forces: A critical study of the SkM force, Nucl. Phys. A **386**, 79 (1982).

[62] J. Dobaczewski, H. Flocard, and J. Treiner, Hartree-Fock-Bogolyubov description of nuclei near the neutron-drip line, Nucl. Phys. A **422**, 103 (1984).

[63] E. Chabanat, P. Bonche, P. Haensel, J. Meyer, and R. Schaeffer, A Skyrme parametrization from subnuclear to neutron star densities Part II. Nuclei far from stabilities, Nucl. Phys. A **635**, 231 (1998).

[64] P. Klüpfel, P.-G. Reinhard, T. J. Bürvenich, and J. A. Maruhn, Variations on a theme by Skyrme: A systematic study of adjustments of model parameters, Phys. Rev. C **79**, 034310 (2009).

[65] M. Kortelainen, T. Lesinski, J. Moré, W. Nazarewicz, J. Sarich, N. Schunck, M. V. Stoitsov, and S. Wild, Nuclear energy density optimization, Phys. Rev. C **82**, 024313 (2010).

[66] M. R. Mumpower, G. C. McLaughlin, and R. Surman, Formation of the rare-earth peak: Gaining insight into late-time r-process dynamics, Phys. Rev. C **85**, 045801 (2012).

[67] L. Neufcourt, Y. Cao, W. Nazarewicz, and F. Viens, Bayesian approach to model-based extrapolation of nuclear observables, Phys. Rev. C **98**, 034318 (2018).

[68] S. A. Giuliani, G. Martínez-Pinedo, and L. M. Robledo, Fission properties of superheavy nuclei for r-process calculations, Phys. Rev. C **97**, 034323 (2018).

[69] A. Bulgac, S. Jin, K. J. Roche, N. Schunck, and I. Stetcu, Fission dynamics of ^{240}Pu from saddle to scission and beyond, Phys. Rev. C **100**, 034615 (2019).